

Flow-induced phase separation of active particles is controlled by boundary conditions

Shashi Thutupalli*

*Simons Centre for the Study of Living Machines, National Centre for Biological Sciences,
GKVK Campus, Bellary Road, Bangalore 560065, India*

International Centre for Theoretical Sciences, Tata Institute of Fundamental Research, Bangalore 560012, India

*Department of Mechanical and Aerospace Engineering, Princeton University, Princeton, NJ 08544, USA and
Joseph Henry Laboratories of Physics, Princeton University, Princeton, NJ 08544, USA*

Delphine Geyer and Howard A. Stone

Department of Mechanical and Aerospace Engineering, Princeton University, Princeton, NJ 08544, USA

Rajesh Singh and Ronojoy Adhikari

The Institute of Mathematical Sciences-HBNI, CIT Campus, Chennai 600113, India and

DAMTP, Centre for Mathematical Sciences, University of Cambridge, Wilberforce Road, Cambridge CB3 0WA, UK

Active particles, including swimming microorganisms, autophoretic colloids and droplets, are known to self-organize into ordered structures at fluid-solid boundaries. The entrainment of particles in the attractive parts of their spontaneous flows has been postulated as a possible mechanism underlying this phenomenon. Here, combining experiments, theory and numerical simulations, we demonstrate the validity of this flow-induced ordering mechanism in a suspension of active emulsion droplets. We show that the mechanism can be controlled, with a variety of resultant ordered structures, by simply altering hydrodynamic boundary conditions. Thus, for flow in Hele-Shaw cells, metastable lines or stable traveling bands can be obtained by varying the cell height. Similarly, for flow bounded by a plane, dynamic crystallites are formed. At a no-slip wall the crystallites are characterised by a continuous out-of-plane flux of particles that circulate and re-enter at the crystallite edges, thereby stabilising them. At an interface where the tangential stress vanishes the crystallites are strictly two-dimensional, with no out-of-plane flux. We rationalize these experimental results by calculating, in each case, the slow viscous flow produced by the droplets and the dissipative, long-ranged, many-body active forces and torques between them. The results of numerical simulations of motion under the action of the active forces and torques are in excellent agreement with experiments. Our work elucidates the mechanism of flow-induced phase separation (FIPS) in active fluids, particularly active colloidal suspensions, and demonstrates its control by boundaries, suggesting new routes to geometric and topological phenomena in active matter.

There are many instances, drawn from biological, physico-chemical and technological contexts, in which microscopic particles produce spontaneous flow in a viscous fluid. The energy necessary to maintain this flow is supplied by a variety of mechanisms, of which there are a wide variety, at the interface between the particles and the fluid. The ciliary layer in cells [1], the chemically reacting boundary layer in autophoretic colloids [2], and the dissolution layer in auto-osmophoretic drops [3] provide three distinct examples. In each case, the activity within the layer drives the exterior fluid into motion which appears as if it were a spontaneous fluid flow around the particles. It is possible, though not necessary, for the particles to translate and/or rotate in response to the spontaneous flow. Irrespective of the property of self-propulsion and/or self-rotation, such active particles in a suspension will each produce a spontaneous flow in which other particles will be entrained. This mutual entrainment, if sufficiently strong, can produce states of organization with no analogue in an equilibrium suspension of passive particles.

The above-mentioned mechanism has been conjectured [4] to underlie the spontaneous crystallization of Janus particles [5] and fast moving bacteria [6] at a plane wall. However, a conclusive experimental demonstration of the validity of this

flow-induced phase separation (FIPS) mechanism is still lacking. If bulk hydrodynamic flow is the principal cause of self-organization, any alteration of the flow should manifest itself in altered states of self-organization. The simplest way of altering the bulk flow, keeping other experimental conditions constant, is to vary the hydrodynamic conditions at the boundaries of the flow. If this produces correspondingly distinct states of self-organization, both the FIPS mechanism and the role of boundaries in controlling it are, thereby, established.

Here, we use a suspension of active, self-propelled emulsion droplets to investigate the role of hydrodynamics on their collective behavior. The system has been used previously [3, 7–10] to provide insights into out-of-equilibrium phenomena relevant to self-organization in both natural [6, 11, 12] and synthetic active particle settings. The typical size $b \sim 50 \mu\text{m}$ of the emulsion droplets and their typical self-propulsion speed $v_s \sim 5 \mu\text{m/s}$ implies that the Reynolds number $Re = v_s b / \nu \sim 10^{-4}$ in a fluid with the kinematic viscosity ν of water. Fluid inertia is negligible at such small Re and the flow is described by the Stokes equation. It is then possible to exploit the linearity of the governing equations and use Green's function techniques to compute the flow, the stress in the fluid, and the forces and torques between the droplets for a variety of boundary condi-

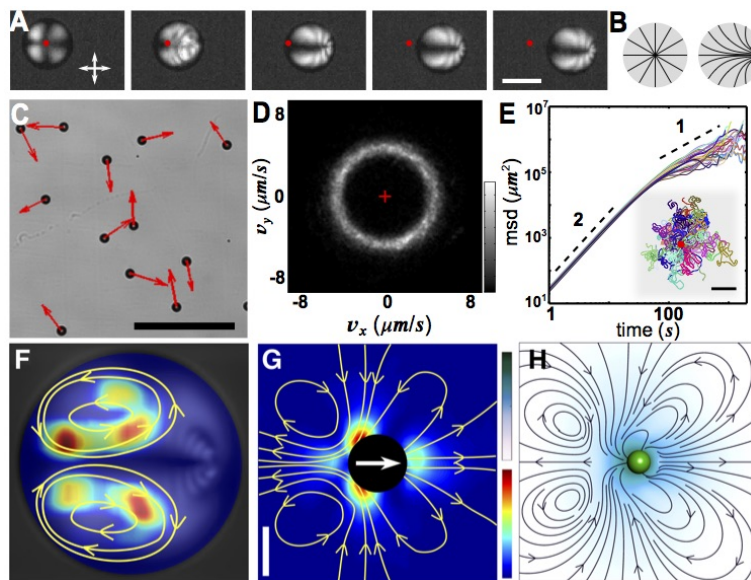


Figure 1. Active droplets made with nematic liquid crystals. **A**. Cross polarisation microscopy images showing spontaneous symmetry breaking and propulsion of an active droplet. The red dot marks the initial position of the active droplet. Each frame is 4 seconds apart. Scale bar is $50\ \mu\text{m}$. **B**. A sketch of the nematic director field (black lines) inside the droplet due to homeotropic anchoring conditions at the interface before (hedgehog defect in the center) and after the symmetry breaking (escaped radial configuration). **C**. Active droplets in a Hele-Shaw cell (height $50\ \mu\text{m}$, which is also the diameter of the droplets; the lateral dimensions of the cell extend beyond the field of view and are $4\ \text{cm} \times 3\ \text{cm}$). Scale bar is $500\ \mu\text{m}$. The red arrows indicate the instantaneous velocities of the droplets. **D**. The probability distribution, using $\sim 10^7$ measurements, of the velocity vectors (v_x, v_y) for individual droplets in a Hele-Shaw geometry. Colorbar represents the normalised probability. **E**. The mean squared displacements calculated from the trajectories of a dilute suspension of active droplets (areal fraction of droplets is $< 0.5\%$). Inset: A superposition of the trajectories of the droplets with their point of origin aligned (marked by red spot). Scale bar is $1\ \text{mm}$. **F**. The rearrangement of the director field inside a droplet swimming to the right is caused by a spontaneous flow inside the droplet. **G**. Experimentally measured external fluid flow for an active droplet (marked by black circle) moving at a fixed velocity. **H**. The theoretical flow from a truncated spherical harmonic expansion, with the expansion coefficient estimated from the experimental flow in **G**. The droplet diameter in **F** and **G** is $50\ \mu\text{m}$ and the colorbars represent the normalized logarithm of the local flow speed.

tions. We find distinct states of aggregation as the boundary conditions are altered, which both validates the conjectured hydrodynamic mechanism and opens up a route to its manipulation and control.

We should note the effect of steric confinement of active fluids on self-organization has been studied thoroughly in the past [13–17]. This knowledge has been exploited in applications such as self-assembly, meta-material synthesis and active fluid computation [18–20]. However the resultant hydrodynamic effects of confinement can be distinct due to difference, for instance, in the slip properties of the boundaries even when the geometry of the confinement is identical. Our work suggests an independent route to ordered states of active matter by using boundaries to alter the *hydrodynamic interactions in*, rather than the *confinement of*, the system. With this remark we now turn to our results.

Experimental system and theoretical model

Our experimental system is an active emulsion of monodisperse droplets of liquid crystal (5CB) in water whose source of activity is droplet dissolution [8]. Surface tension gradi-

ents at the interface of the droplet, sustained by the free energy of dissolution, produce active hydrodynamic flows both within and external to the droplet, leading to droplet motion. While this self-propulsion does not rely on the liquid crystallinity of the droplet, the nematic state of 5CB within it enables the internal velocity field to be inferred (Fig. 1A and Movie S1). The presence of surfactant at the interface makes it energetically favorable for the rod-like 5CB molecules to orient normal to it. Such a homeotropic boundary condition on the director field enforces a point defect, which is located at the center of the droplet (Fig. 1B) when surface tension gradients (and hence fluid flow) are negligible. When observed in polarised light between cross-polarizers, the droplet shows a four-lobed pattern (left-most panel of Fig. 1A) reflecting the symmetric orientation of the director field about the droplet center. When surface tension gradients become appreciable, viscous stresses and fluid flow are induced in the bulk, and so the nematic stress within the droplet must be redistributed. The resulting reorientation of the director causes a displacement of the point defect along the axis of droplet motion and the centro-symmetric four-lobed pattern is distorted to another with a reduced symmetry, now only about the propulsion axis (Fig. 1A, B).

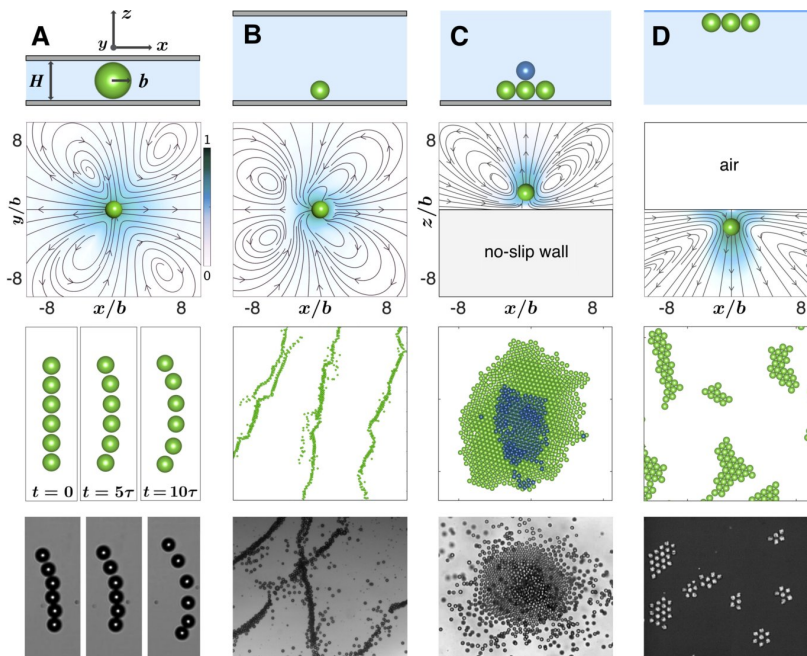


Figure 2. The role of boundaries in determining the collective behaviour of active droplets (particles). Top row: Schematic of confinement. Second row: The exterior flow field produced by the active particles in each boundary condition considered. Third and fourth (bottom) rows, respectively, contain snapshots from simulations and experiments. Traveling lines of active droplets can be formed in a Hele-Shaw cell. These lines are metastable i.e. they translate a few droplet diameters before breaking up, if the separation H of the cell is approximately equal to the droplet diameter (A, $H/b \sim 2$), while these lines are stable when the separation is a few droplet diameters (B, $H/b \sim 8$). Aggregation of the droplets, leading to crystallization, is observed at a plane wall (C, cell depth $H/b \sim 400$) and at the air-water interface (D, cell depth $H/b \sim 400$). At a plane wall, droplets are expunged from the crystalline core, while the crystal is stabilized by the recirculation of the fluid flow. At the air-water interface, on the other hand, there is no out-of-plane motion. Here $\tau = b/v_s$ is the time in which the active droplet moves a distance equal to its radius.

Each droplet propels in a random direction set by its own internal spontaneously broken symmetry and these directions are distributed isotropically (shown in Fig. 1C for the case of a quasi two-dimensional Hele-Shaw cell). The droplet speed (Fig. 1D) is set by its size and the concentration of the surfactant in the external phase [8]. In such a configuration, individual droplets exhibit random, diffusive-like motion due to the fluctuations in the self-propulsion mechanism and due to interactions with the other droplets (Fig. 1E). The balance between viscous and nematic stresses within the droplet tends to align the velocity field with the director field (Fig. 1F) [21], resulting in an asymmetry in the circulatory flow inside the droplets (Movie S2), with a stagnation point close to the point defect. This asymmetry also appears in the external flow generated by the droplets, as can be seen in the velocity field (Fig. 1G) due to a droplet moving with speed v_s . It is in this external flow that other particles are entrained and is, therefore, the focus of our theoretical model.

Our theoretical model for an active particle is a sphere of radius b with an active slip prescribed at its surface. As our primary interest is in the external flow, we assume the internal flow to be a rigid body motion. The fluid velocity on the boundary of the i -th sphere, then, is

$$\mathbf{v}(\mathbf{R}_i + \boldsymbol{\rho}_i) = \mathbf{V}_i + \boldsymbol{\Omega}_i \times \boldsymbol{\rho}_i + \mathbf{v}_i^{\mathcal{A}}(\boldsymbol{\rho}_i), \quad (1)$$

where \mathbf{R}_i is the center of the sphere, $\boldsymbol{\rho}_i$ is a point on its surface with respect to the center and \mathbf{V}_i and $\boldsymbol{\Omega}_i$ are, respectively, its linear and angular velocity. The active slip, $\mathbf{v}_i^{\mathcal{A}}(\boldsymbol{\rho}_i)$, is taken to be the most general surface vector field consistent with incompressibility. Neither axial symmetry of the slip about the orientation axis, \mathbf{p}_i , of the sphere nor flow purely tangential to the interface is assumed. These assumptions distinguish our model [4, 22–24] from that of the classical squirmer [25, 26]. The translational and rotational velocities of the spheres are not known *a priori* but must be determined in terms of the slip velocities from a balance of all forces and torques acting on them.

Slip induces flow in the exterior fluid and the stresses thus produced act back on the sphere surface with a force per unit area \mathbf{f} . Then $\mathbf{F}_i^H = \int \mathbf{f} dS_i$ and $\mathbf{T}_i^H = \int \boldsymbol{\rho}_i \times \mathbf{f} dS_i$ are the net hydrodynamic force and torque on sphere i , which include contributions from the usual Stokes drag, proportional to \mathbf{V}_i and $\boldsymbol{\Omega}_i$, and from the active stresses, proportional to $\mathbf{v}_i^{\mathcal{A}}$. The force per unit area is computed from the solution of the Stokes equation satisfying Eq. 1 at the sphere surfaces and the appropriate hydrodynamic boundary conditions at the exterior boundaries. For our purpose, the boundary integral representation of Stokes flow is most suited for obtaining the force per unit area, as the hydrodynamic boundary conditions can be directly applied by choosing a suitable Green's function. We employ

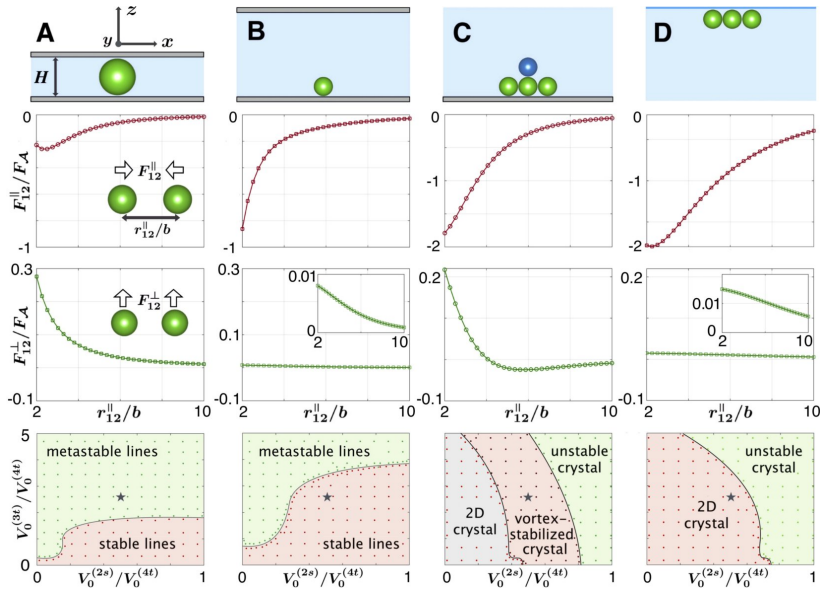


Figure 3. Active forces on the active particles are modified by the presence of boundaries. Second row: Attractive parallel forces lead to the formation of traveling lines in a Hele-Shaw cell (**A** and **B**), and aggregation in the plane of the wall (**C**) and the interface (**D**). Third row: The perpendicular forces in a Hele-Shaw cell are an order of magnitude larger for **A**, and accounts for the metastable lines in this case. The perpendicular force at the plane wall is ten times larger than the corresponding force at the interface and results in the circulatory motion of active particles (see text for more details). Insets show close-up and $F_{\mathcal{A}} = 6\pi\eta b v_s$. Bottom row: State diagrams in terms of the strengths of the slip modes - $V_0^{(2s)}$: symmetric dipole, $V_0^{(3t)}$: vector quadrupole, and $V_0^{(4t)}$: degenerate octupole. Each dot represents a simulation, while the star denotes the values used in the above rows.

this approach here and analytically solve the resulting integral equations for the force per unit area, to leading order in sphere separation, in a basis of tensorial spherical harmonics with appropriate Green's functions. The forces and torques thus obtained are inserted into force and torque balance equations that are integrated numerically to obtain the translational and rotational motions of the spheres (further details of the model and simulations are in the *SI Appendix*).

The free parameters in our model, the sphere radius b_i and the slip velocity $v_i^{\mathcal{A}}$, are determined as follows. We set $b_i \sim 50 \mu\text{m}$ which is the measured radius of an undissolved droplet. There is less than 1% change to this value during the course of the experiment. We use the exterior flow of a single droplet to determine the slip, as the two are uniquely related for any given hydrodynamic boundary condition. We parametrize $v_i^{\mathcal{A}}$ in terms of its first three tensorial harmonic coefficients, as these fully account for the long-ranged components of the exterior flow. We then estimate the coefficients by minimizing the square deviation between the experimentally measured flow and the three mode expansion. The exterior flow thus obtained (Fig. 1H) is in good agreement with the experimentally measured flow (Fig. 1G). We note that the flow in the Hele-Shaw cell is used for this estimation and comparison.

To emphasise, we fit the *one-body* exterior flow to estimate the active slip and then use it to *predict* the *many-body* exterior flow and the many-body forces and torques for any given boundary condition. We note that the three-mode expansion is not a limitation of the theoretical model, which accommodates

as many modes as may be necessary to represent the exterior flow to the desired level of accuracy.

Self-organization and boundary conditions

We now present the main results on the correspondence between self-organization of active particles and hydrodynamic boundary conditions. Our boundary conditions are (i) a plane channel flow in a Hele-Shaw cell where the channel width H is approximately one particle diameter (Fig. 2A), (ii) a plane channel flow where the channel width varies between several particle diameters ($H \sim 6 - 10b$, Fig. 2B), (iii) flow bounded by a plane wall where the flow vanishes (Fig. 2C) and (iv) flow bounded by a plane air-water interface where the tangential stress vanishes (Fig. 2D). In every case, the emulsion parameters are kept unchanged; the *only* change is in the exterior boundary conditions.

Snapshots from the experiments (bottom row, Fig. 2) point to distinct signatures of the boundary conditions on the resultant self-organization of the droplets. In the Hele-Shaw cell, $H \sim 2b$, droplets spontaneously form metastable lines, which curve in their direction of motion and eventually break up after traversing a few droplet diameters (Fig. 2A and Movie S3). Increasing the channel width, $H \sim 8b$, transforms these lines into surprisingly stable bands that travel through each other even as they collide (Fig. 2B and Movie S4). In contrast, at a plane wall, droplets form crystallites parallel to the plane. Droplets comprising the crystallite are constantly expelled

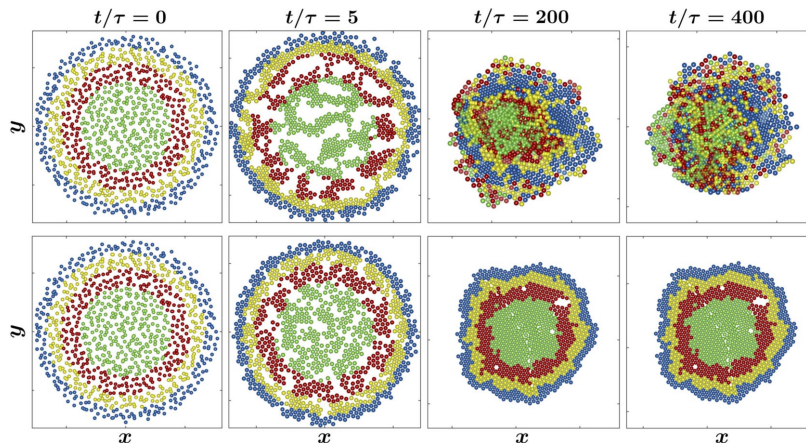


Figure 4. Kinetics of aggregation of active particles at a plane wall (top row) and at a plane interface (bottom row). The colors are used to indicate and track the particles based on their initial positions. The instantaneous snapshots show that there is a faster mixing of particles and exchange of neighbors at the plane wall due to the circulatory flow streamlines (Fig. 2C) and higher values of perpendicular forces (Fig. 3C).

from the center of the aggregate only to rejoin it at the edges. The recirculating flows ensure a balanced in and out-flux of the droplets and thereby maintain a constant mean droplet number within these aggregates (vortex-stabilised crystallites, Fig. 2C, Movie S5). When the plane wall is replaced by a plane interface, the previous inflow and outflow is suppressed and the droplets form two-dimensional crystalline aggregates. These aggregates are maintained in a steady state by a continuous coagulation and fragmentation of the crystallites (Fig. 2D, Movie S6).

A qualitative understanding of these states of self-organization is obtained from the *one-body* external flow of the particle in each of the four boundary conditions (corresponding panels of Fig. 2). We emphasize, once again, that in this calculation the active slip is *estimated* from flow in the Hele-Shaw cell but used to *predict* flow for the three remaining boundary conditions. Operationally, the latter only requires the use of the appropriate Green's function. In the Hele-Shaw cell, the net flow is parallel to the walls and has an inflowing component perpendicular to the direction of motion. Entrainment in this inflow leads to the formation of metastable lines and stable bands. At both the plane wall and the plane interface, the flow has a cylindrical symmetry when the propulsion axis is perpendicular to the plane. In the first case, the flow has a strong circulation in which entrained particles are drawn inwards along the plane but then expelled normal to it. In the second case, the circulatory component is comparatively weak and entrained particles are primarily drawn inwards. Entrainment in this flow leads to the formation, respectively, of vortex-stabilised crystallites and of coagulating and fragmenting two-dimensional crystallites. The qualitative agreement of the simulations (third row, Fig. 2) obtained from the numerical integration of the force and torque balance equations with experiment (bottom row, Fig. 2) is excellent. This agreement between experiment and theory that disregards the internal flow confirms, *a posteriori*, our hypothesis that entrainment in the external flow is primarily responsible for self-organization.

A quantitative understanding of the states of self-organization requires an accurate estimate of the forces and torques between particles. We calculate the components of the active pair force parallel and perpendicular to their separation vector, as a function of separation distance, for each of the four boundary conditions considered (second and third rows, Fig. 3). In each of the cases, the component of the active force parallel to the separation vector is negative and it is this attractive component of the active force that leads to aggregation. However, there is a considerable variation in the component of the active force perpendicular to the separation vector, and it is the sensitivity of this component to boundary conditions that accounts for the variety of the aggregated states. In the Hele-Shaw cell, the perpendicular force is positive which, in our sign convention, means that it is directed along the direction of motion. Since to leading order, hydrodynamic forces are pair-wise additive, this implies that the net force on particles at the center of a moving line are greater than those at the edges. Therefore, they tend to move faster, creating a curvature of the line and eventually its break up. In contrast, the perpendicular force in the plane channel is an order of magnitude smaller (as shown in the corresponding inset of Fig. 3B for clarity) and the break up mechanism has a negligible contribution, which gives the traveling bands their surprisingly stability. At a no-slip wall (Fig. 3C), the perpendicular force is negative at large distances but positive at short distances. This drives particles into the wall when they are well-separated but away from the wall when they are close by. Combined with the parallel component of the flow, which is always attractive, this leads to the expulsion and re-circulation of particles in the crystalline aggregate. In contrast, the perpendicular force at an interface, (Fig. 3D) is positive, but an order of magnitude smaller (again, shown in the inset for clarity) and the dominant motion is due to the attractive component of the parallel force. Thus, expulsion is suppressed and the result is the formation of two-dimensional crystallites. Similar estimates for the torque provide an understanding of the orientational dy-

namics which is relatively unimportant in our case as Brownian re-orientation is negligible and the hydrodynamic torques are one power of separation smaller than the corresponding forces.

Since each irreducible mode of the slip is independent of the others and produces flow of distinct multipolar symmetry, it is possible to isolate the effect of each mode on the self-organization. The modes are labelled by an angular momentum index $l = 0, 1, 2, \dots$ and a spin index $\sigma = s, a, t$ corresponding to the symmetric, antisymmetric and pure trace irreducible components of each mode. Using the abbreviation $l\sigma$ to indicate a mode with angular momentum index l and spin index σ , the $3t$ mode produces self-propulsion (and a degenerate quadrupolar flow) while the $2s$ mode produces inflow and outflow along mutually perpendicular axes (and a dipolar flow). The latter is the stresslet mode and its instantaneous sign determines if the fluid is being expelled (“pusher”) or ingested (“puller”) along the propulsion axis. We are then able to construct a state-diagram in the $V_0^{(2s)} - V_0^{(3t)}$ plane that demarcates regions of stability of the principal states of aggregation found for each of the four boundary conditions studied (Fig. 3, bottom row). In Hele-Shaw flow, the stresslet mode promotes stability but in flows bounded by a plane wall, the perpendicular component of the force is enhanced in proportion to the magnitude of the stresslet, which leads from two-dimensional crystallites to vortex-stabilised crystallites and finally to instabilities. Thus, by suitably choosing the strength of the stresslet mode, it is possible to select either a state of two-dimensional crystals or vortex-stabilised crystals. For flow bounded by an interface, an enhanced stresslet mode does not lead to expulsion of the droplets out-of-plane but directly to an instability (unstable crystallites).

Our results above provide convincing evidence of the mechanism of hydrodynamic entrainment in the spontaneous exterior flow as the dominant mechanism for self-organization in active particles. The active parts of the hydrodynamic forces and torques that result from this entrainment provide both a qualitative and quantitative explanation of the states of self-organization. These hydrodynamic forces and torques depend on the distance between the particles, on their orientation, and the magnitudes of the modes of the slip on each active particle. It can be directly verified from the explicit forms of the forces and torques that they cannot be obtained as gradients of potentials [18]. Further, their dependence on the modes of the slip velocity indicates that they have odd parity under time reversal, signaling their explicitly dissipative nature [4, 24]. Thus, we have a novel situation in which long-range, *dissipative* forces and torques promote self-organization. States of self-organization maintained by entropy production were studied in the past by the Brussels school and were given the name *dissipative structures* [27]. Self-organization in active particles, as shown here, appears to be an example of a dissipative structure but one in which the dissipative mechanism and the resultant forces and torques are unambiguously identified.

Kinetics of flow-induced phase separation

The self-organization presented above can be viewed, from the point of view of statistical physics, as a phase separation phenomenon driven by dissipative forces, rather than the usual conservative forces derived from a potential. The study of such flow-induced phase separation (FIPS) presents several challenges, one of which is to determine a quantity that can serve as the analogue of a thermodynamic potential. It appears from recent theoretical work that large-deviation results for the stationary distribution of Markov processes violating detailed balance may provide a tractable route for answering questions of stability [28]. Here we draw attention to the fact that kinetic routes to similar flow-induced phase-separated states may vary depending on the boundary condition. This is borne out in the differences between the kinetics of phase separation at a plane wall and at a plane interface (Fig. 4 and Movie S7). At a plane wall, there is both an enhanced mixing within the crystal plane and an exchange of neighbors due to the closed streamlines (Fig. 2C) and higher values of perpendicular forces (Fig. 3C) compared to the plane interface. In a biological context, such hydrodynamic bound structures and associated kinetics could influence the encounter rate of individuals in aggregates [6, 29].

Discussion

The flow-induced phase separation (FIPS) mechanism established here and conjectured earlier [4] has several distinguishing features that bear pointing out and contrasting with other mechanisms. First, self-propulsion and/or self-rotation are *not* necessary for its operation; it is only necessary that the particles produce a long-ranged exterior hydrodynamic flow. The experimentally observed states of self-organization persist even when the self-propulsion parameter $V_0^{(3t)}$ vanishes (state diagrams, bottom row of Fig. 3). Second, in the absence of thermal fluctuations, the suspension is mechanically unstable to aggregation at any positive value of the density and any finite amount of activity, however small. It is plausible that in the presence of thermal fluctuations, finite values of density and activity are required to overwhelm the loss in entropy due to aggregation. A careful study of aggregation at different temperatures, densities and activities is needed to establish this quantitatively. Third, FIPS includes as a special case, aggregation in driven colloidal systems which are nonetheless force and torque free [30, 31]. Fourth, the long-lived, stable traveling bands that we have shown here are qualitatively different as compared to other dynamic behavior seen in active systems [18, 32, 33] or in the emergence of orientational order in flocking models [34]. In spite of the similarity in the aggregated states, the hydrodynamic mechanism identified here is distinct. Fifth, our work provides an understanding of phase-separation in active systems that is complementary to motility-induced phase separation (MIPS) [35]. The latter has a kinematic character, in which the flux of particles is

a prescribed functional of density, reflecting the tendency of active particles to slow down or speed up in regions of, respectively, higher or lower density. The physics underlying this tendency is left implicit, and may plausibly be attributed to non-hydrodynamic interactions, like contact, compression, or jamming. In contrast, FIPS has an explicitly dynamic character, as forces and torques of hydrodynamic origin are identified in causing the aggregation. It is entirely conceivable that a state of aggregation like hexagonal crystallites can be formed from either of these mechanisms. On the other hand, vortex-stabilised crystallites appear difficult to explain within MIPS whereas they appear naturally in FIPS. Since FIPS needs a wall with no slip or an interface with vanishing tangential stress, aggregate structures that remain stable away from such boundaries would point to a mechanism such as MIPS as the source of stability. Finally, though our experiments are performed with droplets, the theory and simulation correspond to arbitrary active particles and our flow boundary conditions are generic to many natural and engineered settings. Together, these underscore the importance of our findings to a wide class of active fluids, in particular active colloids, and to the study and control of geometric and topological phenomena in active matter.

Acknowledgements

We thank T. Tlustý, M.E. Cates and R. E. Goldstein for discussions. S.T. acknowledges the Human Frontier Science Program (Cross Disciplinary Fellowship) for funding. R.A. thanks the IUSSTF for supporting a sabbatical visit to Princeton University. R.S and R.A. acknowledge the Institute of Mathematical Sciences for computing resources on the Nandadevi clusters.

SUPPLEMENTARY INFORMATION (SI)

Experimental methods

Our experimental system is comprised of thousands of monodisperse liquid crystal-in-water emulsion droplets. The droplet phase is the liquid crystal 4-pentyl-cyano-biphenyl (5CB). The drops have a uniform radius in the range $b = 35 - 50 \mu\text{m}$ and are immersed in an external water phase containing Sodium Dodecyl Sulfate (SDS), which is at a concentration [5 to 20% weight/weight(w/w)] much greater than its critical micellar concentration (CMC). The presence of surfactant at such high concentrations causes a spontaneous dissolution of the droplet [36], the result of which is sustained motion of the droplets. The direction of motion is due to a spontaneously broken symmetry [8], which is dynamically sustained by the dissolution instability leading to an interfacial tension gradient around the droplet. As a result, the droplets translate through the aqueous background at speeds in the range of $v_s \sim 3 - 20 \mu\text{m}/\text{s}$.

Active forces and torques

The details of our dynamical model for the active spheres, including long-ranged, many-body hydrodynamic interactions in the presence of boundaries, are described below. The spherical active droplet is modeled as an active sphere with a slip velocity $\mathbf{v}_i^{\mathcal{A}}$ on its surface, as shown in Eq.(1). We expand the slip as

$$\mathbf{v}_i^{\mathcal{A}}(\mathbf{R}_i + \boldsymbol{\rho}_i) = \sum_{l=1}^{\infty} \frac{1}{(l-1)!(2l-3)!!} \mathbf{V}_i^{(l)} \cdot \mathbf{Y}^{(l-1)}(\hat{\boldsymbol{\rho}}_i), \quad (\text{S1})$$

in the irreducible basis of tensorial spherical harmonics $\mathbf{Y}^{(l)}(\hat{\boldsymbol{\rho}}_i) = (-1)^l \rho_i^{l+1} \nabla^{(l)} \rho_i^{-1}$, where $\nabla^{(l)} = \nabla_{\alpha_1} \dots \nabla_{\alpha_l}$, and ρ_i denotes the radius vector of i -th particle. The expansion coefficients $\mathbf{V}_i^{(l)}$ are l -th rank reducible Cartesian tensors. They can be written in terms of three irreducible parts $\mathbf{V}_i^{(l\sigma)}$ of ranks l , $l-1$, and $l-2$ respectively, corresponding to the symmetric traceless ($\sigma = s$), antisymmetric ($\sigma = a$) and pure trace ($\sigma = t$) parts. The first two modes of the slip, $\mathbf{V}_i^{(1s)} \equiv -\mathbf{V}_i^{\mathcal{A}}$ and $\mathbf{V}_i^{(2a)} \equiv -b\boldsymbol{\Omega}_i^{\mathcal{A}}$, are respectively the active translational velocity and active angular velocity for a sphere in an unbounded medium [22, 37, 38]. Explicitly, they are

$$\mathbf{V}_i^{\mathcal{A}} = -\frac{1}{4\pi b^2} \int \mathbf{v}_i^{\mathcal{A}}(\boldsymbol{\rho}_i) dS_i, \quad (\text{S2a})$$

$$\boldsymbol{\Omega}_i^{\mathcal{A}} = -\frac{3}{8\pi b^4} \int \boldsymbol{\rho}_i \times \mathbf{v}_i^{\mathcal{A}}(\boldsymbol{\rho}_i) dS_i. \quad (\text{S2b})$$

Given the slip, we seek expressions for the hydrodynamic forces \mathbf{F}_i^H and torques \mathbf{T}_i^H on the spheres. By linearity of Stokes flow, it is clear that these must be of the form

$$\mathbf{F}_i^H = -\gamma_{ij}^{TT} \cdot \mathbf{V}_j - \gamma_{ij}^{TY} \cdot \boldsymbol{\Omega}_j - \sum_{l\sigma=1s}^{\infty} \gamma_{ij}^{(T,l\sigma)} \cdot \mathbf{V}_j^{(l\sigma)}, \quad (\text{S3a})$$

$$\mathbf{T}_i^H = -\gamma_{ij}^{RT} \cdot \mathbf{V}_j - \gamma_{ij}^{RR} \cdot \boldsymbol{\Omega}_j - \sum_{l\sigma=1s}^{\infty} \gamma_{ij}^{(R,l\sigma)} \cdot \mathbf{V}_j^{(l\sigma)}, \quad (\text{S3b})$$

where repeated particle indices are summed over and Cartesian indices, implicit in the bold-face notation, are fully contracted. The $\gamma_{ij}^{\alpha\beta}$ with $(\alpha, \beta = T, R)$ are the usual Stokes friction tensors [39–41], while the $\gamma_{ij}^{(T,l\sigma)}$ and $\gamma_{ij}^{(R,l\sigma)}$ are friction tensors associated with the slip [4, 24]. Explicit forms of these generalized friction tensors can be obtained from the solution of the boundary integral equation of the Stokes problem, in terms of Green's function satisfying the appropriate boundary conditions [4, 24]. In general, the tensors are long-ranged, many-body functions of Stokes flow and encode the dissipative hydrodynamic interactions between the active spheres mediated by the intervening fluid. Brownian forces on swimmers are typically $O(k_B T/b) \approx 10^{-16}$ N, while the typical active forces on our swimmers are of the order $F_{\mathcal{A}} = 6\pi\eta b v_s \approx 10^{-11}$ N. Thus, the active hydrodynamic forces are orders of magnitude larger than the Brownian forces, and

we therefore ignore the effects of thermal fluctuations in the fluid. The translational and rotational motions of the spheres are then found by setting the net hydrodynamic forces and torques to zero.

Rigid body motion of active colloids

. Using the above expressions for the forces and torques in Newton's equations and inverting the linear system for the velocities and angular velocities yields explicit dynamical equations for the rates of change of positions and orientations:

$$\mathbf{V}_i = \boldsymbol{\mu}_{ij}^{TT} \cdot \mathbf{F}_j + \boldsymbol{\mu}_{ij}^{TR} \cdot \mathbf{T}_j + \sum_{l\sigma=2s}^{\infty} \boldsymbol{\pi}_{ij}^{(T,l\sigma)} \cdot \mathbf{V}_j^{(l\sigma)} + \mathbf{V}_i^{\mathcal{A}}, \quad (\text{S4a})$$

$$\boldsymbol{\Omega}_i = \boldsymbol{\mu}_{ij}^{RT} \cdot \mathbf{F}_j + \boldsymbol{\mu}_{ij}^{RR} \cdot \mathbf{T}_j + \sum_{l\sigma=2s}^{\infty} \boldsymbol{\pi}_{ij}^{(R,l\sigma)} \cdot \mathbf{V}_j^{(l\sigma)} + \boldsymbol{\Omega}_i^{\mathcal{A}}. \quad (\text{S4b})$$

These are the principal dynamical equations of our model. Here, $\boldsymbol{\mu}_{ij}^{\alpha\beta}$ are the familiar mobility matrices [41], while the propulsion tensors $\boldsymbol{\pi}_{ij}^{(\alpha,l\sigma)}$, first introduced in [23], relate the rigid body motion to modes of the active slip. They are given in terms of the mobility matrices and the generalized friction tensors [24],

$$-\boldsymbol{\pi}_{ij}^{(T,l\sigma)} = \boldsymbol{\mu}_{ik}^{TT} \cdot \boldsymbol{\gamma}_{kj}^{(T,l\sigma)} + \boldsymbol{\mu}_{ik}^{TR} \cdot \boldsymbol{\gamma}_{kj}^{(R,l\sigma)}, \quad (\text{S5a})$$

$$-\boldsymbol{\pi}_{ij}^{(R,l\sigma)} = \boldsymbol{\mu}_{ik}^{RT} \cdot \boldsymbol{\gamma}_{kj}^{(T,l\sigma)} + \boldsymbol{\mu}_{ik}^{RR} \cdot \boldsymbol{\gamma}_{kj}^{(R,l\sigma)}. \quad (\text{S5b})$$

The propulsion tensors inherit the long-ranged, many-body character of the generalized friction tensors and play a role analogous to the mobility matrices. A method of calculating them directly, without requiring inversion of the generalized friction tensors, has been provided in [23]. The solution is obtained in terms of a Green's function of Stokes equation.

We now list the Green's functions used for the various geometries explored in the experiment.

(a) *Plane no-slip wall*: We use the Lorentz-Blake Green's function [42] for swimmers near a no-slip wall. The Lorentz-Blake tensor satisfies the no-slip condition at a plane wall. We write it as

$$G_{\alpha\beta}^w(\mathbf{R}_i, \mathbf{R}_j) = G_{\alpha\beta}^o(\mathbf{R}_i - \mathbf{R}_j) + G_{\alpha\beta}^*(\mathbf{R}_i, \mathbf{R}_j^*), \quad (\text{S6})$$

where $G^o(\mathbf{r}) = (\nabla^2 \mathbf{I} - \nabla \nabla) \frac{\mathbf{r}}{8\pi\eta}$ is the Oseen tensor and $G^*(\mathbf{R}', \mathbf{R}^*)$ is the correction, due to the image system, necessary to satisfy the boundary condition at the no-slip wall. The expression for the correction to Green's function near a plane wall is

$$G_{\alpha\beta}^* = \frac{1}{8\pi\eta} \left[-\frac{\delta_{\alpha\beta}}{r^*} - \frac{r_{\alpha}^* r_{\beta}^*}{r^{*3}} + 2h^2 \left(\frac{\delta_{\alpha\nu}}{r^{*3}} - \frac{3r_{\alpha}^* r_{\nu}^*}{r^{*5}} \right) \mathcal{M}_{\nu\beta} - 2h \left(\frac{r_{\alpha}^* \delta_{\alpha\nu} + \delta_{\nu\beta} r_{\alpha}^* - \delta_{\alpha\beta} r_{\nu}^*}{r^{*3}} - \frac{3r_{\alpha}^* r_{\nu}^* r_{\beta}^*}{r^{*5}} \right) \mathcal{M}_{\nu\beta} \right]. \quad (\text{S7})$$

The correction is obtained from the image of the swimmer with respect to the wall located at $\mathbf{R}^* = \mathcal{M} \cdot \mathbf{R}$, where $\mathcal{M} = \mathbf{I} - 2\hat{z}\hat{z}$ is the mirror operator. Here $\mathbf{r} = \mathbf{R}_i - \mathbf{R}_j$, $\mathbf{r}^* = \mathbf{R}_i - \mathbf{R}_j^*$, and h is the height of the swimmer from the wall. The coordinate system is described in Fig. (S1).

(b) *Plane free-slip interface*: We use the Green's function obtained by Aderogba and Blake [43] for swimmers near a free-slip air-water interface

$$G_{\alpha\beta}^s(\mathbf{R}_i, \mathbf{R}_j) = G_{\alpha\beta}^o(\mathbf{r}) + (\delta_{\beta\alpha\rho} \delta_{\alpha\rho\gamma} - \delta_{\beta 3} \delta_{3\gamma}) G_{\alpha\gamma}^o(\mathbf{r}^*). \quad (\text{S8})$$

(c) *Parallel plane no-slip walls*: The Green's functions for Stokes flow between parallel, planar no-slip walls has been obtained by several authors. In the Hele-Shaw limit, where the separation between the walls is of the order of the diameter of the swimmer, $H \sim 2b$, we use an approximate form of the Green's function [44]

$$G_{\alpha\beta}^{2w}(\mathbf{R}_i, \mathbf{R}_j) = \frac{3hz(H-z)(H-h)}{\pi\eta H^3} \left(\frac{\delta_{\alpha\beta}}{2r_{\parallel}^2} - \frac{r_{\alpha} r_{\beta}}{r_{\parallel}^4} \right). \quad (\text{S9})$$

Here r_{\parallel} is a measure of the distances in the plane parallel to the walls.

At larger separations, $H \sim 10b$, we use the solution of [45], which employs a series sum of the Lorentz-Blake tensor. This is given as

$$G_{\alpha\beta}^{2w}(\mathbf{R}_i, \mathbf{R}_j) = G_{\alpha\beta}^o(\mathbf{R}_i, \mathbf{R}_j) + G_{\alpha\beta}^*(\mathbf{R}_i, \mathbf{R}_j^{b*}) + G_{\alpha\beta}^*(\mathbf{R}_i, \mathbf{R}_j^{t*}) + G_{\alpha\beta}^{\delta}. \quad (\text{S10})$$

Here \mathbf{R}_j^{b*} and \mathbf{R}_j^{t*} are the images of the swimmer at \mathbf{R}_j due to the bottom and top walls respectively. $G_{\alpha\beta}^{\delta}$ is the additional contribution required to satisfy the boundary conditions at the two walls. This is approximate by a series sum of the Lorentz-Blake tensor, Eq. (S6), about the two walls.

Estimation of the slip flow

. Given the slip, the fluid flow is obtained exactly in terms of the boundary integral representation of Stokes flow. Briefly, the flow is expressed as an infinite series of boundary integrals, each integral corresponding to a mode of the slip, and these integrals are evaluated exactly in terms of the Green's function of Stokes flow, making use of its biharmonic property [23, 24, 46]. The experimental flow is well-approximated by a truncated version of the slip expansion of Eq.(S1) which retains the following three leading terms

$$\mathbf{v}_i^{\mathcal{A}}(\boldsymbol{\rho}_i) = -\mathbf{V}_i^{\mathcal{A}} + \frac{1}{15} \mathbf{V}_i^{(3t)} \cdot \mathbf{Y}^{(2)}(\boldsymbol{\rho}_i) + \mathbf{V}_i^{(2s)} \cdot \mathbf{Y}^{(1)}(\boldsymbol{\rho}_i) - \frac{1}{75} \mathbf{V}_i^{(4t)} \cdot \mathbf{Y}^{(3)}(\boldsymbol{\rho}_i). \quad (\text{S11})$$

This includes contributions from $l\sigma = 2s, 3t$ and $4t$ modes of the slip, which correspond respectively to flows with dipolar, degenerate quadrupolar, and quadrupolar symmetry. We use uniaxial parametrization of the slip coefficients in terms

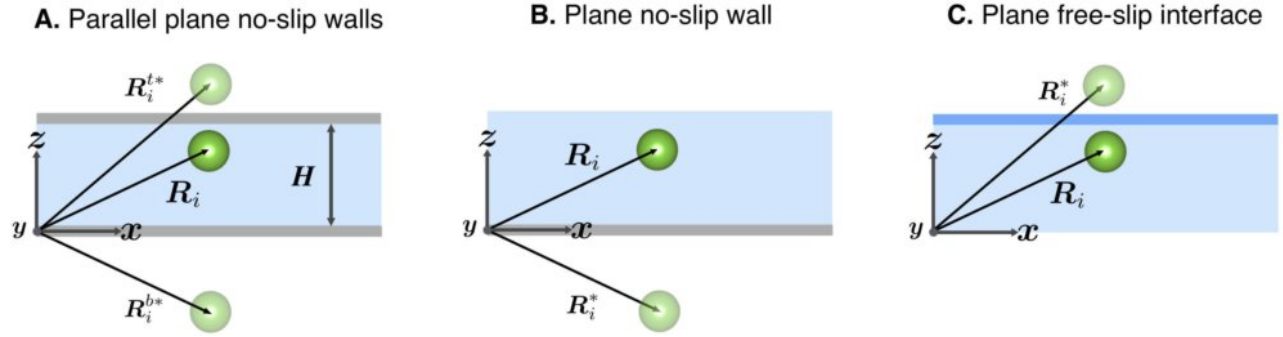


Figure S1. The coordinate system used to describe the i -th spherical active colloid and its image in following geometries of flow: A. parallel no-slip plane walls, B. plane no-slip wall, and C. plane free-slip surface. See the text for details

of the particle orientation \mathbf{p}_i as: $\mathbf{V}_i^{\mathcal{A}} = v_s \mathbf{Y}^{(1)}(\mathbf{p}_i)$, $\mathbf{V}_i^{(2s)} = V_0^{(2s)} \mathbf{Y}^{(2)}(\mathbf{p}_i)$, $\mathbf{V}_i^{(3t)} = V_0^{(3t)} \mathbf{Y}^{(1)}(\mathbf{p}_i)$, and $\mathbf{V}_i^{(4t)} = V_0^{(4t)} \mathbf{Y}^{(2)}(\mathbf{p}_i)$ where $Y_\alpha^{(1)}(\mathbf{p}) = p_\alpha$ and $Y_{\alpha\beta}^{(2)}(\mathbf{p}) = p_\alpha p_\beta - \frac{1}{3} \delta_{\alpha\beta}$. The strengths of the modes - $V_0^{(2s)} = 0.05$, $V_0^{(3t)} = 0.25$, and $V_0^{(4t)} = 0.10$ - are determined by fitting the experimental and the theoretical fluid flows. The above form of the slip is then used to obtain the flow and the forces and torques necessary to update the positions and orientations of the swimmers in different geometries.

Simulation Details.

The simulations are performed by numerical integration of Eq. (S4), where the series sum is truncated based on the minimal model of the active slip in Eq. (S11). The coefficients of slip expansion are chosen to ensure that the theoretical flow field is qualitatively similar to the experimentally measured flow field. These parameters are then kept fixed for all the simulations reported. The evaluation of the rigid body motion of the colloids and the flow disturbance created by them has been performed using PyStokes [47]. The numerical integration of the resulting equations are performed using an adaptive time step integrator, which uses the backward differentiation formula [48]. Random packing of hard-spheres [49] is used as the initial distribution of particles in all the simulations. The colloid-colloid and the colloid-wall repulsive interaction is modeled using the short-ranged repulsive WCA potential [50], which is given as, $U(r) = \epsilon \left(\frac{r_{min}}{r}\right)^{12} - 2\epsilon \left(\frac{r_{min}}{r}\right)^6 + \epsilon$, for $r < r_{min}$ and zero otherwise, where ϵ is the potential strength. The WCA parameters for particle-particle repulsion are: $r_{min} = 4.4$, $\epsilon = 0.08$, while for the particle-wall repulsion we choose $r_{min} = 2.4$, $\epsilon = 0.08$. The number of particles N used, for respective plots, are: Fig. (2A): $N = 6$; Fig. (2B): $N = 900$; Fig. (2C), (2D), (4A), and (4B): $N = 1024$. Other parameters used in the simulations are: radius of particle ($b = 1$), self-propulsion speed $v_s = 0.15$, the strength of the bottom-heaviness ($T_0 = 0.2$) and dynamic viscosity $\eta = 0.1$. The phase diagrams of Fig. (3) are obtained using $N = 16$ particles for

panels (A) and (B), while $N = 128$ particles have been used to obtain panels (C) and (D). These parameters have been used in generating all the figures except the phase diagrams of Fig. (3), where strengths of the symmetric irreducible dipole and vector quadrupole have been varied to map the phase diagram.

* shashi@ncbs.res.in

- [1] Brennen, C & Winet, H. (1977) Fluid mechanics of propulsion by cilia and flagella. *Annu. Rev. Fluid Mech.* **9**, 339–398.
- [2] Ebbens, S. J & Howse, J. R. (2010) In pursuit of propulsion at the nanoscale. *Soft Matter* **6**, 726–738.
- [3] Thutupalli, S, Seemann, R, & Herminghaus, S. (2011) Swarming behavior of simple model squirmers. *New J. Phys.* **13**, 073021.
- [4] Singh, R & Adhikari, R. (2016) Universal hydrodynamic mechanisms for crystallization in active colloidal suspensions. *Phys. Rev. Lett.* **117**, 228002.
- [5] Palacci, J, Sacanna, S, Steinberg, A. P, Pine, D. J, & Chaikin, P. M. (2013) Living crystals of light-activated colloidal surfers. *Science* **339**, 936–940.
- [6] Petroff, A. P, Wu, X.-L, & Libchaber, A. (2015) Fast-moving bacteria self-organize into active two-dimensional crystals of rotating cells. *Phys. Rev. Lett.* **114**, 158102–158106.
- [7] Thutupalli, S & Herminghaus, S. (2013) Tuning active emulsion dynamics via surfactants and topology. *Eur. Phys. J. E* **36**, 9905.
- [8] Herminghaus, S, Maass, C. C, Krüger, C, Thutupalli, S, Goehring, L, & Bahr, C. (2014) Interfacial mechanisms in active emulsions. *Soft Matter* pp. 7008–7022.
- [9] Izri, Z, Linden, M. N. V. D, & Dauchot, O. (2014) Self-propulsion of pure water droplets by spontaneous marangoni-stress-driven motion. *Phys. Rev. Lett.* **248302**, 1–5.
- [10] Shani, I, Beatus, T, Bar-Ziv, R. H, & Tlusty, T. (2014) Long-range orientational order in two-dimensional microfluidic dipoles. *Nat. Phys.* **10**, 1–5.
- [11] Cavagna, A & Giardina, I. (2014) Bird flocks as condensed matter. *Annu. Rev. Condens. Matter Phys.* **5**, 183–207.
- [12] Sokolov, A, Aranson, I, Kessler, J, & Goldstein, R. (2007) Concentration dependence of the collective dynamics of swimming bacteria. *Phys. Rev. Lett.* **98**, 1–4.
- [13] Woodhouse, F. G & Goldstein, R. E. (2012) Spontaneous circulation of confined active suspensions. *Phys. Rev. Lett.* **109**,

- 168105.
- [14] Wioland, H, Woodhouse, F. G, Dunkel, J, Kessler, J. O, & Goldstein, R. E. (2013) Confinement stabilizes a bacterial suspension into a spiral vortex. *Phys. Rev. Lett.* **110**, 268102.
- [15] Bricard, A. et. al. (2015) Emergent vortices in populations of colloidal rollers. *Nat. Commun.* **6**, 7470.
- [16] Solon, A. P. et. al. (2015) Pressure is not a state function for generic active fluids. *Nat. Phys.* **11**, 673.
- [17] Y. Fily, A. Baskaran, M. H. (2014) Dynamics of self-propelled particles under strong confinement. *Soft Matter* **10**, 5609–5617.
- [18] Niu, R, Palberg, T, & Speck, T. (2017) Self-assembly of colloidal molecules due to self-generated flow. *Phys. Rev. Lett.* **119**, 028001.
- [19] Souslov, A, van Zuiden, B. C, Bartolo, D, & Vitelli, V. (2017) Topological sound in active-liquid metamaterials. *Nat. Phys.*
- [20] Woodhouse, F. G & Dunkel, J. (2017) Active matter logic for autonomous microfluidics. *Nat. Commun.* **8**, 15169.
- [21] Prishchepa, O. O, Shabanov, A. V, & Zyryanov, V. Y. (2005) Director configurations in nematic droplets with inhomogeneous boundary conditions. *Phys. Rev. E* **72**, 1–11.
- [22] Ghose, S & Adhikari, R. (2014) Irreducible representations of oscillatory and swirling flows in active soft matter. *Phys. Rev. Lett.* **112**, 118102.
- [23] Singh, R, Ghose, S, & Adhikari, R. (2015) Many-body microhydrodynamics of colloidal particles with active boundary layers. *J. Stat. Mech* **2015**, P06017.
- [24] Singh, R & Adhikari, R. (2018) Generalized Stokes laws for active colloids and their applications. *J. Phys. Commun.* **2**, 025025.
- [25] Lighthill, J. M. (1952) On the squirming motion of nearly spherical deformable bodies liquids at very small reynold number. *Comm. Pure Appl. Maths.*(5) **5**, 108–118.
- [26] Blake, J. R. (1971) A spherical envelope approach to ciliary propulsion. *J. Fluid Mech.* **46**, 199–208.
- [27] Kondepudi, D & Prigogine, I. (1998) *Modern thermodynamics: from heat engines to dissipative structures*. (John Wiley & Sons).
- [28] Touchette, H. (2009) The large deviation approach to statistical mechanics. *Phys. Rep.* **478**, 1–69.
- [29] Drescher, K, Leptos, K. C, Tuval, I, Ishikawa, T, Pedley, T. J, & Goldstein, R. E. (2009) Dancing volvox: Hydrodynamic bound states of swimming algae. *Phys. Rev. Lett.* **102**, 1–4.
- [30] Negi, A. S, Sengupta, K, & Sood, A. K. (2005) Frequency-dependent shape changes of colloidal clusters under transverse electric field. *Langmuir* **21**, 11623–11627.
- [31] Sapozhnikov, M. V & et. al. (2003) Dynamic self-assembly and patterns in electrostatically driven granular media. *Phys. Rev. Lett.* **90**, 114301.
- [32] Schaller, V, Weber, C, Semmrich, C, Frey, E, & Bausch, A. R. (2010) Polar patterns of driven filaments. *Nature* **467**, 73–77.
- [33] Ohta, T & Yamanaka, S. (2014) Traveling bands in self-propelled soft particles. *Eur. Phys. J. ST* **223**, 1279–1291.
- [34] Solon, A. P, Chaté, H, & Tailleur, J. (2015) From phase to microphase separation in flocking models: The essential role of nonequilibrium fluctuations. *Phys. Rev. Lett.* **114**, 068101.
- [35] Cates, M. E & Tailleur, J. (2015) Motility-induced phase separation. *Annu. Rev. Condens. Mat. Phys.* **6**, 219–244.
- [36] Peddireddy, K, Kumar, P, Thutupalli, S, Herminghaus, S, & Bahr, C. (2012) Solubilization of thermotropic liquid crystal compounds in aqueous surfactant solutions. *Langmuir* **28**, 12426–12431.
- [37] Anderson, J & Prieve, D. (1991) Diffusiophoresis caused by gradients of strongly adsorbing solutes. *Langmuir* **7**, 403–406.
- [38] Stone, H. A & Samuel, A. D. T. (1996) Propulsion of microorganisms by surface distortions. *Phys. Rev. Lett.* **77**, 4102–4104.
- [39] Ladd, A. J. C. (1988) Hydrodynamic interactions in a suspension of spherical particles. *J. Chem. Phys.* **88**, 5051–5063.
- [40] Mazur, P & van Saarloos, W. (1982) Many-sphere hydrodynamic interactions and mobilities in a suspension. *Physica A: Stat. Mech. Appl.* **115**, 21–57.
- [41] Kim, S & Karrila, S. J. (1992) *Microhydrodynamics: Principles and Selected Applications*. (Butterworth-Heinemann).
- [42] Blake, J. R. (1971) A note on the image system for a stokeslet in a no-slip boundary. *Proc. Camb. Phil. Soc.* **70**, 303–310.
- [43] Aderogba, K. (1976) On stokeslets in a two-fluid space. *J. Eng. Math.* **10**, 143–151.
- [44] Liron, N & Mochon, S. (1976) Stokes flow for a stokeslet between two parallel flat plates. *J. Eng. Math.* **10**, 287–303.
- [45] Staben, M. E, Zinchenko, A. Z, & Davis, R. H. (2003) Motion of a particle between two parallel plane walls in low-Reynolds-number Poiseuille flow. *Phys. Fluids* **15**, 1711–1733.
- [46] Singh, R & Adhikari, R. (2017) Fluctuating hydrodynamics and the Brownian motion of an active colloid near a wall. *Eur. J. Comp. Mech* **26**, 78–97.
- [47] Singh, R, Laskar, A, & Adhikari, R. (2014) Pystokes: Hampi.
- [48] Langtangen, H. P & Wang, L. (2012) Odespy.
- [49] Skoge, M, Donev, A, Stillinger, F. H, & Torquato, S. (2006) Packing hyperspheres in high-dimensional euclidean spaces. *Phys. Rev. E* **74**, 041127.
- [50] Weeks, J. D, Chandler, D, & Andersen, H. C. (1971) Role of repulsive forces in determining the equilibrium structure of simple liquids. *J. Chem. Phys.* **54**, 5237–5247.